Additive manufacturing of Proton-Conducting Ceramics by robocasting with integrated laser postprocessing

Joanna Pośpiech [a,*], Małgorzata Nadolska [a], Mateusz Cieślik [a], Tomasz Sobczyk [a], Marek Chmielewski [a], Aleksandra Mielewczyk-Gryń [a], Ragnar Strandbakke [b,c], José Manuel Serra [d], Sebastian Lech Wachowski [a]

[a] Institute of Nanotechnology and Materials Engineering, Faculty of Applied Physics and Mathematics, Advanced Materials Centre, Gdańsk University of Technology, Poland
[b] Department of Chemistry, Centre for Materials Science and Nanotechnology, University of Oslo, Norway
[c] SINTEF Industry, Sustainable Energy Technology, Oslo, Norway
[d] Instituto de Tecnología Química, Universitat Politècnica de València – Consejo Superior de Investigaciones Científicas, av. Los Naranjos sn, 46022 Valencia, Spain

ARTICLE INFO

ABSTRACT

A hybrid system combining robocasting and NIR laser postprocessing has been designed to fabricate layers of mixed proton-electron conducting $Ba_{0.5}La_{0.5}Co_{1-x}Fe_xO_{3-\delta}$ ceramic. The proposed manufacturing technique allows for the control of the geometry and microstructure and shortens the fabrication time to a range of a few minutes. Using 5 W laser power and a scanning speed of 500 mm·s^{-1}, sintering of a round-shaped layer with an 8 mm radius was performed in less than 2 s. The single phase of the final product was confirmed by X-ray diffraction. Various ceramic-to-polymer weight ratios were tested, showing that various porosities of microstructures of ~30 - 35 % and ~19 % can be obtained with 2:1 and 4:1 loading respectively.

1. Introduction

Protonic Conducting Ceramics (PCCs) gained a lot of interest in recent years due to their possible application in the field of energy conversion and storage as elements of the Protonic Ceramic Electrochemical Cells (PCECs) [1–4]. The two most basic applications of PCCs are the Proton Ceramic Electrolysers (PCEs) and Protonic Ceramic Fuel Cells (PCFCs). The former produce hydrogen via steam electrolysis [5], while in the latter the opposite process occurs in which the reaction of hydrogen fuel with oxygen produces water, heat and electric power [6]. Moreover, PCEs enable the electrochemical hydrogen pumping [7,8]. The utilization of proton-conducting oxides as base elements of PCECs allows for operation at intermediate temperatures (400 – 600 °C), reducing thermal and chemical degradation [9,10]. As the process of the water formation occurs on the air side, the fuel dilution is prevented. In recent years of development, the applications of the PCECs with a high efficiencies were demonstrated [2–4,11]. The presented applications for energy systems, however, still stay only at the lab-scale level. The commercialization of PCECs could benefit from automated fabrication processes, especially for the fabrication of all the elements of the device in a single process.

One of the problems, for a highly sufficient fabrication process, stems from a difference in the sintering temperatures of each constituent of the device (e.g. <1200 °C for the electrodes and >1400 °C for electrolytes) [12–14]. Moreover, a different microstructure is required for each element. For instance, the electrode must be designed with a porous microstructure to allow the gas penetration to enhance the reaction area of all the species (protons, electrons, and oxygen) happening on its side. The electrolyte, on the other hand, must be of high density to prevent gas leakage from both sides of the device. Another challenge is the variety of desired geometries of the devices. The majority of the laboratory tests are performed on button cells, although there are more and more reports on novel ideas for the shapes of PCECs elements [15] or whole devices [13,16,17]. Additive manufacturing presents a viable solutions to this combination of challenges. 3D printing techniques show the possibility of creating complex structures (stacks, desired microarchitectures, and porosity) and customized shapes for specific devices, fast prototyping time, and reduction of production cost [18–20]. The 3D printing of ceramics may have different approaches [21–24]. It can be an extrusion-based method – such as Robocasting (also known as DIW -

---

* Corresponding author.

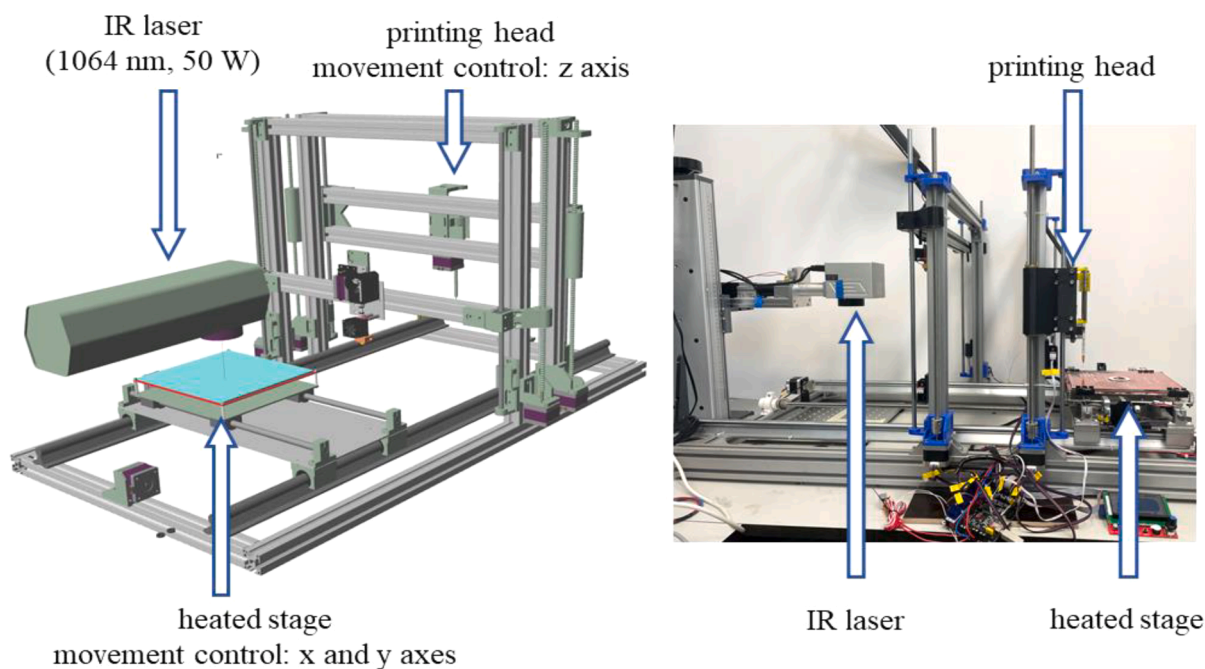*E-mail address:* joanna.pospiech@pg.edu.pl (J. Pośpiech).

Fig. 1. Construction of the printer combining extrusion-based 3D printing technology and laser postprocessing.

Direct Ink Writing) – where a plasticized material of polymer-ceramic composite is deposited on desired surface [18,25,26]. The ink extrusion must be coherent to obtain continuous printout structures. Another approach to ceramic 3D printing are methods utilizing powder ceramic beds, where an organic binder is applied, connecting the desired ceramic structures in the polymerization process [27–29]. In both techniques, high-temperature postprocessing is utilized to remove organic additives and sinter a ceramic structure, making it difficult to co-sinter PCEC elements with different sintering temperatures. Some techniques avoids furnace postprocessing by utilizing laser heat treatment of the powder ceramic, e.g. Selective Laser Sintering (SLS) [18,30–32]. In those methods, ceramic powders are scanned with a laser beam, which locally creates high temperature and sinter or melt the ceramic powder with improved control of geometry and microstructure. Additionally, as typical scanning speeds are in the range of 100-1000 mm·s^{-1}, the process of sintering is very fast compared to classical sintering. SLS gives lower energy consumption as the laser can be used with power of a few watts, but cannot directly fabricate subsequent elements of different compositions. However, the prospect of laser sintering of ceramics is a great breakthrough and has been successfully applied for the fabrication of dense electrolytes, porous electrodes, dense interconnectors, and dense mixed protonic and electronic-conduction composites [33–36].

A combination of extrusion-based 3D printing with laser heat treatment integrates the following advantages: control of the geometry, microstructure and thickness of printouts, formation of local high temperatures that can be adjusted to specific compositions, and what gives the biggest breakthrough, shortening the time of fabrication from days to even seconds due to easy prototyping and fast post-processing. Additionally, the shortened sintering time significantly reduces energy consumption, lowering costs and making the process more eco-friendly.

Herein we focused on development of the new fabrication technique of PCC elements. $Ba_{0.5}La_{0.5}Co_{0.25}Fe_{0.75}O_{3-\delta}$ (BLCF75) – a promising PCEC positrode material [37,38] – was used as testing material. The compound selection of the PCEC electrode must take into account the essential property of this element, which is the conductivity of the charge carries that drive the processes, namely electrons or electron holes, oxide ions, and protons. Cobaltites and ferrites with perovskite structures exhibit both high electronic conductivity ($\sigma_{el} > 100$ S·cm^{-1}) and oxide ionic conductivity [38–41]. Recently, there has been a

number of research undertaken on the protonic partial conductivity in these compounds involving different substitutions [39,42,43]. Our recent study on $Ba_{0.5}Ln_{0.5}CoO_{3-\delta}$ (Ln stands for lanthanide) has shown that compounds containing La and/or Gd, exhibit higher protonic defect formation [44]. Additionally, research indicates that the basicity of a material and the concentration of protons are correlated, meaning that the substation with the more basic cation might promote the formation of protonic defects [39,42]. Thus, it stands to reason that the concentration of protonic defects in barium lanthanide cobaltites may increase if Co were to be replaced with more basic Fe. The group of materials with the formula $Ba_{0.5}La_{0.5}Co_{1-x}Fe_xO_{3-\delta}$ are currently studied and our studies demonstrates protonic defect formation influencing the electrical conductivity on those materials [45,46]. Additionally, the substitution of Fe for Co lowers the thermal expansion coefficient (TEC) [47], bringing it closer to the TEC of $BaZr_{0.4}Ce_{0.4}Y_{0.2}O_{3-\delta}$, the most often used PCEC electrolyte. This additionally prevents those components from cracking and delaminating, improving the device's mechanical stability.

In this work, we present new technique of additive manufacturing of Proton-Conducting Ceramics by robocasting with integrated laser post-processing. The BLCF75 layers were deposited on disk-shaped $BaZr_{0.4}Ce_{0.4}Y_{0.2}O_{3-\delta}$ electrolyte pellets. Single-phase electrodes of various porosity were fabricated with the developed fabrication technique.

2. Experimental

2.1. Preparation of ink

To create plasticized inks allowing the coherent extrusion of the material, the ceramic powder was dispersed in the polymer matrix. The inks were composed of BLCF75 ceramic powder and polyvinyl alcohol (PVA) water solution. PVA was selected due to its uncomplicated composition, non-toxicity, biodegradability, water solubility, and ease of removal. The crucial property of selected polymer was that the products of its thermal decomposition are primary gaseous water, acetaldehyde, acetic acid, carbon dioxide, methane, and carbon monoxide. This property is essential to prevent the contamination of the ceramics during the firing of the polymer matrix in the laser postprocessing. The ceramic was prepared by solid-state synthesis. The powder precursors: La_2O_3 (pre-annealed for 5 h at 900 °C, 99.9 % Alfa
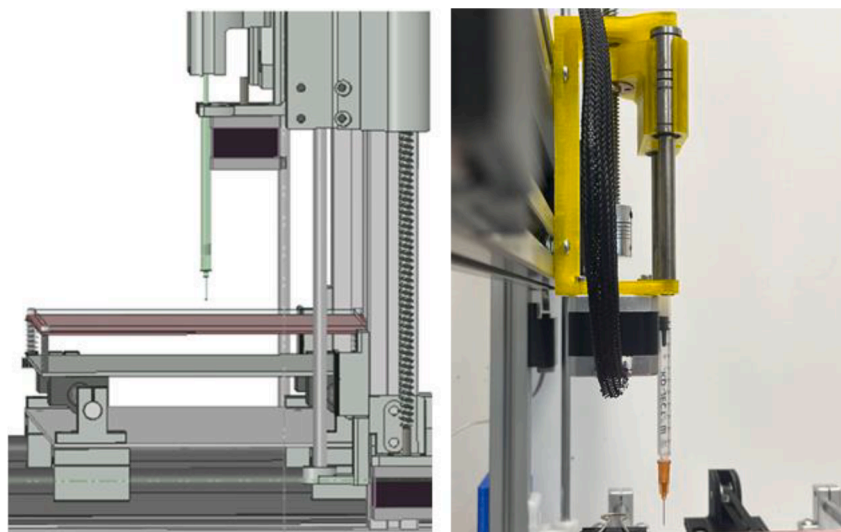
Fig. 2. Construction of the printing head consisted of the 1 ml syringe placed in a special holder that controlled the pressure of the syringe piston by a trapezoid spindle with a step motor.

Aesar), $BaCO_3$ (99.9 % Sigma Aldrich), Co_3O_4 (99.98 % Alfa Aesar), and Fe_2O_3 (99.9 % Alfa Aesar) were mixed in a stoichiometric amounts, ground in a ball mill for 20 h at 450 rpm, pelletized and annealed at 1200 °C for 48 hours. The synthesized ceramic was finally ball milled in isopropyl alcohol for 6 hours at 450 rpm and sieved with a 200 μm sieve to obtain a ceramic powder with uniform grain size. The parameter selection of ball milling was based on our previous work [45]. The PVA powder (88.7 % hydrolyzed, Chempur) was dissolved in deionized water in 10 % ratio under magnetic stirring at 300 rpm. The raw powder was suspended in isopropanol (1 g·ml^{-1}), added to the dissolved PVA, and stirred. Ultrasonication (30 min, 5 W) was used as the homogenization process. The inks were prepared with different PVA to ceramic weight

ratios, respectively, 1:1, 1:2, and 1:4 (50 vol.%, 66.7 vol.%, 80 vol.%, respectively).

2.2. 3D printing device

In this work, a robocasting printer was designed as a Cartesian 3D printer. The printing system consists of an extrusion-based printing head mounted on a gate controlled in the z-axis (15 cm), heating stage controlled in the x (60 cm) and y (16.5 cm) axis, and NIR laser head (1064 nm, 50 W, FIBER Laser DIOLUT) (Fig. 1). The movement of the gate with the printing head is controlled by trapezoid spindles (8 mm diameter; 8 mm lift per rotation), step motors, and optical limit switches
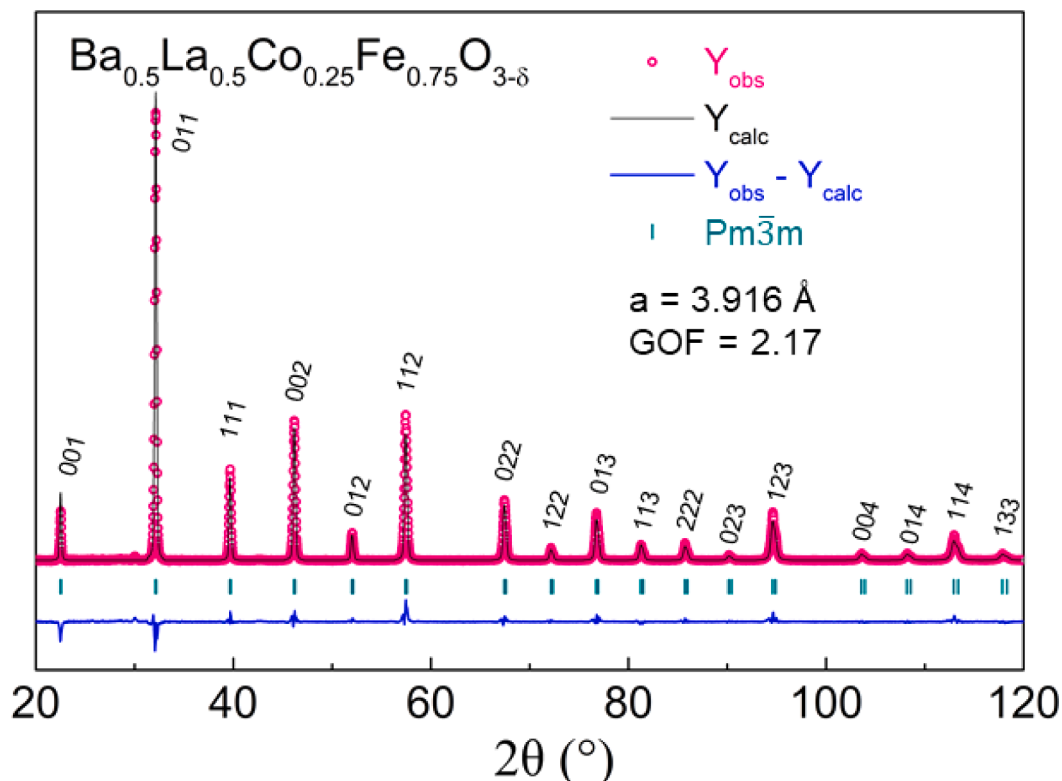

Fig. 3. Diffraction pattern with Rietveld refinement profile of synthesized $Ba_{0.5}La_{0.5}Co_{0.25}Fe_{0.75}O_{3-\delta}$.

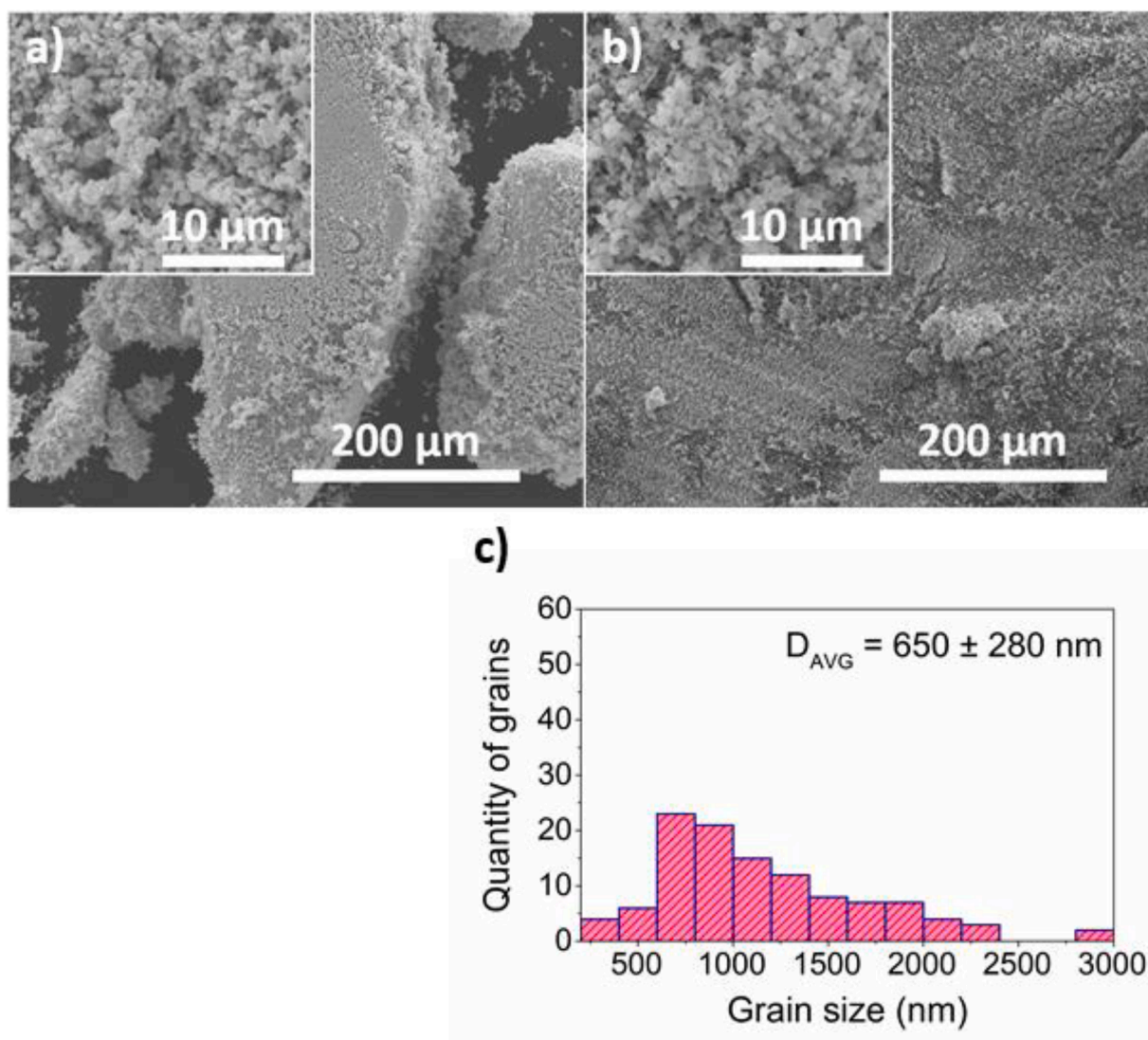**Fig. 4.** SEM images of $Ba_{0.5}La_{0.5}Co_{0.25}Fe_{0.75}O_{3-\delta}$ ceramic powder before (a) and after the ball milling process for 6 h (b); histogram of the average powder grain size of ceramic powder after the ball milling process (c).

on both sides of the gate. The table is controlled by the ball screw on the y-axis, and the timing belt on the x-axis, both working with the step motors and mechanical limit switches. The size of the table 21.5 cm x 21.5 cm gives approximately 19 cm x 19 cm of printable area. Additionally, the table is heated by the 60 W heater (max temperature 100 °C). The printing head consists of the 1 ml syringe placed in a customized holder that controls the pressure of the syringe piston by a trapezoid spindle with a step motor (Fig. 2).

The printer was fully automated and controlled by a computer using controllers based on a BIG TREE TECH motherboard with 32-bit processors. The firmware is based on the open-source MARLIN firmware [48], adjusted for the developed printer system. The NIR laser was mounted next to the printing heads, allowing the table with the printout to move under the laser beam, providing a fast and fully automated printing and sintering process. Detailed technical drawings of the developed devices are given in SI Section 1.

2.3. 3D printing and laser postprocessing

The electrodes were printed on commercially available ~2 mm thick, disk-shaped $BaZr_{0.4}Ce_{0.4}Y_{0.2}O_{3-\delta}$ electrolyte pellets (NorECS, Norway). The distance of the nozzle from the electrolyte was approximately equal

to the thickness of the wet 3D printed layer (~500 μm). The CAD model of printouts was circle-shaped and the printing process was controlled by the UltiMaker Cura software [49]. First, the contour was made and continuously filled line by line with bidirectional movement.

Laser postprocessing was performed with the NIR laser in a continuous mode. The surface of the printouts was scanned line by line with the ~10 μm wide laser beam. The shape of the model and the scanning program was prepared first in the EZCad2 software which controlled the laser head. The idea of the laser sintering of polymer-ceramic composite is to gradually decompose and remove the organics while and simultaneously sinter the ceramic component. Different parameters of laser scanning program were tested as follows: laser power in the range 5 – 10 W, scanning speed 500 – 1000 mm·s^{-1}, working frequency 20 – 40 kHz, and number of scans from 1 to 3. With changing parameters, the energy absorbed by the material on spot was changing, causing different sintering mechanism. Picture of finished product is given in SI Section 2.

2.4. Characterization methods

The morphology of the samples was analyzed with scanning electron microscopy (ESEM Quanta FEG 250, FEI). The porosity of the achieved microstructure was calculated by the contrast-based analysis of SEM
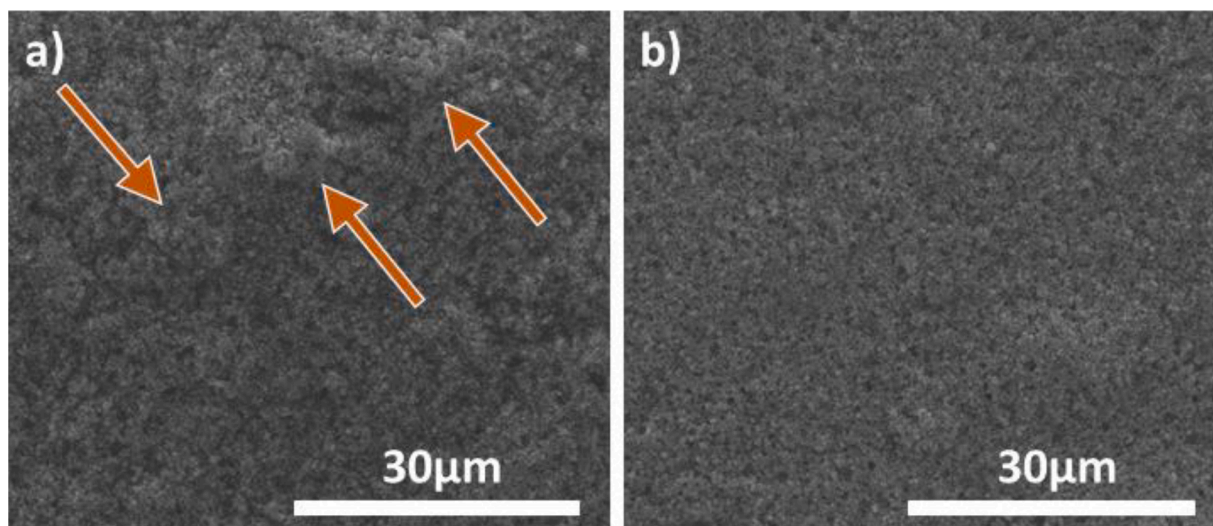
Fig. 5. SEM images of ink with ceramic added in the form of powder (a) and isopropanol suspension (b). The arrows points the agglomeration of grains.

Table 1
Summary of the prepared inks (10 % PVA wt.% solution) with their synthesis parameters.

Sample no.	PVA to ceramic wt. ratio	Viscosity (mPa·s)
1.0	-	196.4
1.1	1:1	481.4
1.2	1:2	366.5
1.4	1:4	326.1

images in the ImageJ program [50]. Powder X-ray Diffraction was used to determine sample composition and quality. X-ray diffractograms were collected at room temperature on a Philips X'Pert Pro diffractometer with Cu-Kα radiation, from 20 to 120°. The rheological studies of prepared inks were performed using Modular Compact Rheometer MCR 302e. The height of the green and sintered layers were calculated from the images obtained with confocal microscopy (Olympus Lext OLS4000).

3. Results and discussion

3.1. Ink preparation

The recorded diffraction pattern with the Rietveld refinement result of BLCF75 sintered powder is shown in Fig. 3. The observed diffraction reflections determine the single-phase cubic perovskite (space group $Pm\bar{3}m$). The Rietveld refinement was performed using the crystallographic data for the cubic unit cell (space group Pm$\bar{3}$m, the number of the space group: 221).

The synthesized ceramic powder had irregular shapes and a wide grain size distribution as shown in the micrograph in Fig. 4a. This renders the as-synthesized powder unsuitable for preparing a homogeneous gel. Post-synthesis ball milling provided a fine powder with grains with an average size of ~0.65 μm and a more homogeneous microstructure (Fig. 4b and c). The powder grain size was calculated via ImageJ and presented in Fig. 4c.

Next, to obtain high homogeneity in the ink, we compared two approaches of mixing ceramic with PVA - adding ceramic powder or powder suspended in isopropanol. SEM analysis confirmed a more uniform dispersion of powder suspended in isopropanol (Fig. 5b), while for the ink with powder, we observed agglomeration of the grains (pointed with arrows in Fig. 5a).

Table 1 summarizes all inks prepared with their synthesis parameters and viscosity results. Selected compositions were tested by extruding with the printing head nozzle and no clogging or abruption in the continuity of the extrusion was observed.

3.2. 3D printing and laser postprocessing

To compare the effect of different ceramic loading in the gel we performed the complete process of printing and laser sintering with the first parameters chosen to be: scanning speed 500 mm·s^{-1}, 20 kHz frequency, 1 scan, and 5 W of laser beam power. SEM micrographs of the printed structures are presented in Fig. 6. As expected, an increase of the ceramic powder in the ink composition increased the density of the obtained microstructures. With the PVP:BLCF75 1:1 ratio (Fig. 6a), the
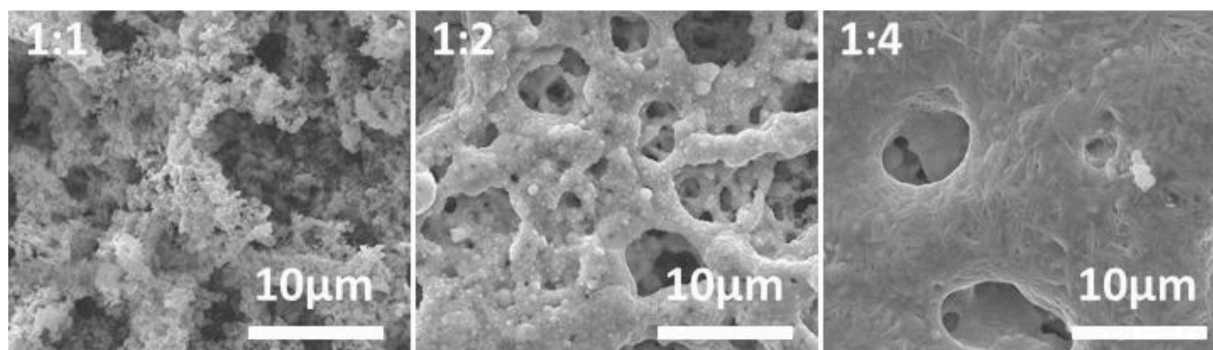

Fig. 6. SEM images of the from inks obtained microstructures of different compositions – PVA to ceramic ratios of 1:1, 1:2 and 1:4.
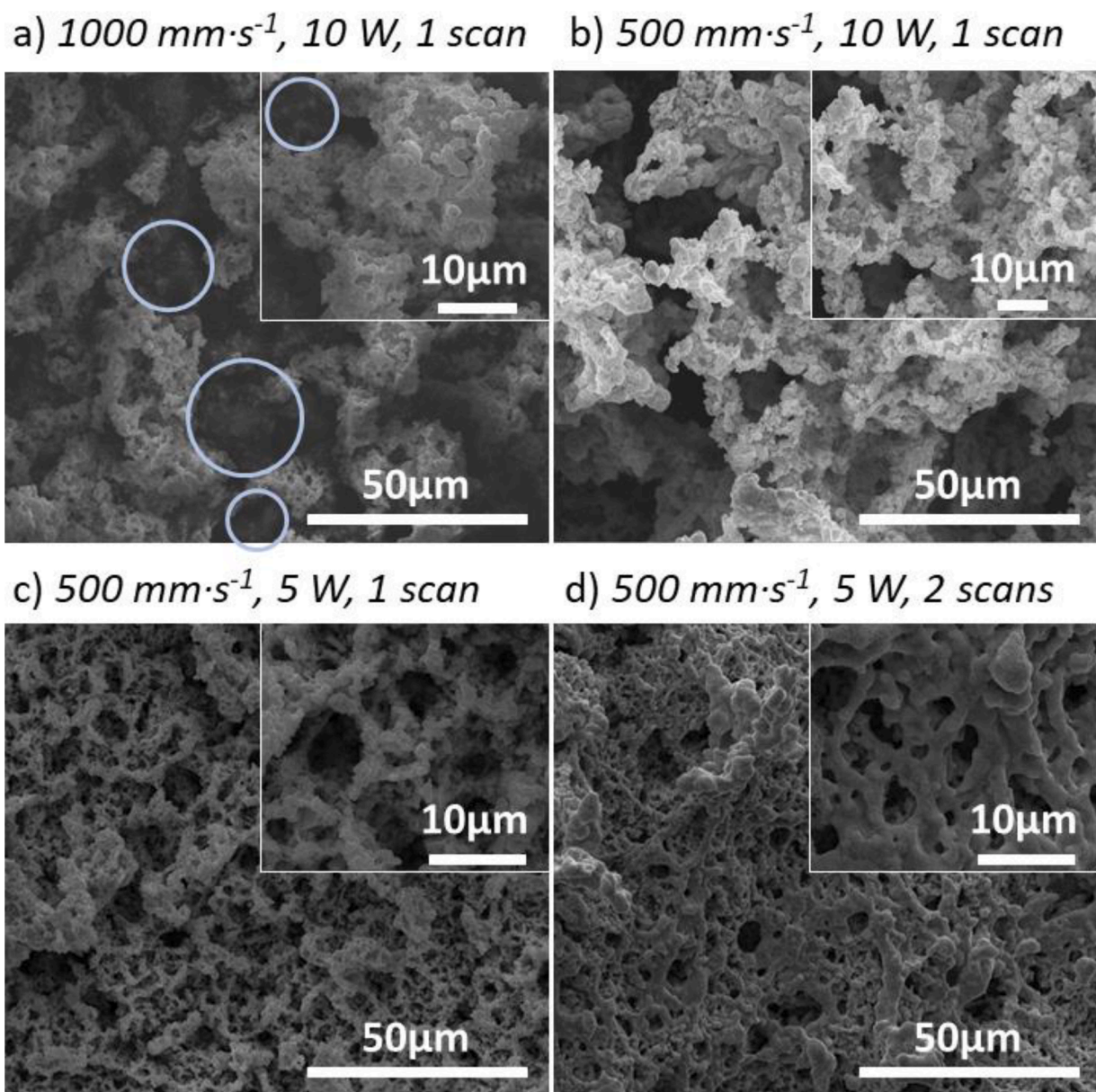
Fig. 7. SEM images of layers sintered with various laser sintering parameters (a) 1000 mm·s^{-1}, 10 W, 1 scan; with circled polymer leftovers; (b) 500 mm·s^{-1}, 10 W, 1 scan; (c) 500 mm·s^{-1}, 5 W, 1 scan; (d) 500 mm·s^{-1}, 5 W, 2 scans.

ceramic powder did not create a visible necking between grains. The 1:2 ratio (Fig. 6b) sintered in the continuous microstructure with visible pores. The porosity calculates from SEM images using ImageJ software yielded value was approximately 30 %, and necking between the grains was observed, indicating a good connection between the ceramic grains. The layer printed with a 1:4 ratio ink had the highest density, with a small number of pores visible on the surface (porosity of ~18.8 %). As the study focused on the development of electrodes, the porous microstructure was desired and the 1:2 ratio ink was selected for further studies. However, the results show that higher density could be manufactured if needed.

The development of a sintering technique with a laser required a thorough study of the selected parameters. Numerous tests were performed to study the influence of each variable such as distance of the laser from the printed layer, speed of laser beam scanning, frequency, and number of scans. The confocal length of the utilized laser was first optimized, and a detailed procedure is given in SI Section 3. The selected distance between the laser head and the printed layer was 223 mm.

The matrix of four layers sintered with changing one variable parameter is presented in Fig. 7. Fig. 7a and 7b present sintered layers with 10 W, one scan, and different scan speeds. With the 1000 mm·s^{-1} speed (Fig. 7a) we observed the leftover polymer matrix (circled on the figure), while with the 500 mm·s^{-1} speed (Fig. 7b) the polymer was completely removed. As the speed of the laser beam scan increases, the time of interaction between the laser beam energy and the material decreases causing a lower local temperature at the spot, which would explain the differences. Even though the polymer was removed during laser processing using 500 mm·s^{-1} scan speed the microstructure of sintered ceramic was still porous showing desired properties of the ceramic electrode material. For all of the presented layers there was no delamination or cracking observed.

To compare the influence of the total power of the laser beam, we compared layers sintered with a scan speed of 500 mm·s^{-1}, 1 scan, and 10 W and 5 W (Fig. 7b and 7c, respectively). In both cases, the polymer matrix was completely removed, and the ceramic was sintered in the continuously connected porous microstructure. We observed that with
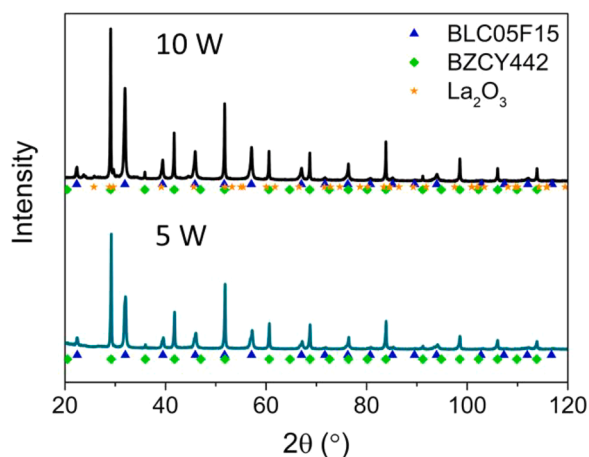
Fig. 8. XRD pattern of $Ba_{0.5}La_{0.5}Co_{0.25}Fe_{0.75}O_{3-\delta}$ samples sintered with 10 W and 5 W laser's power.

an increase in the laser beam total power, the porosity also increases from ~35.2 % for 5W to ~59.5 % for 10 W. As the effect of increased laser power, the ceramic powders sinter in more coarser

microstructures. The layer sintered with a scan speed of 500 mm·s^{-1}, 5 W, was compared with the layer scanned twice with the same parameters (Fig. 7c and 7d). The ceramic grains were sintered more compared with single scan sample, as visible in the inset in Fig. 7d, indicating higher local temperature in the process.

On the two selected specimens - sintered with one scan performed with 500 mm·s^{-1} scan speed and the power laser of 5 W and 10 W, we performed a postprocessing X-ray diffraction analysis (Fig. 8). Both diffractograms showed a major phase of $Ba_{0.5}La_{0.5}Co_{0.25}Fe_{0.75}O_{3-\delta}$ (printed layer) and the phase of $BaZr_{0.4}Ce_{0.4}Y_{0.2}O_{3-\delta}$ electrolyte (substrate below the layer). However, in the case of the layer sintered with 10 W, La_2O_3 peaks were observed. This indicated partial decomposition of the printed layer, probably due to local overheating.

The height profile of the layer sintered with 500 mm·s^{-1} scan speed and the power laser of 5 W layer shown the consistent growth of the printout edge, reaching a uniform thickness of 143(3) μm (Fig. 9).

4. Conclusions

This study developed a system of additive manufacturing of ceramics by combining the robocasting technique with 1064 nm fiber IR laser sintering. The $Ba_{0.5}La_{0.5}Co_{0.25}Fe_{0.75}O_{3-\delta}$ round-shaped layers were successfully printed on the $BaZr_{0.4}Ce_{0.4}Y_{0.2}O_{3-\delta}$ electrolyte and sintered. By
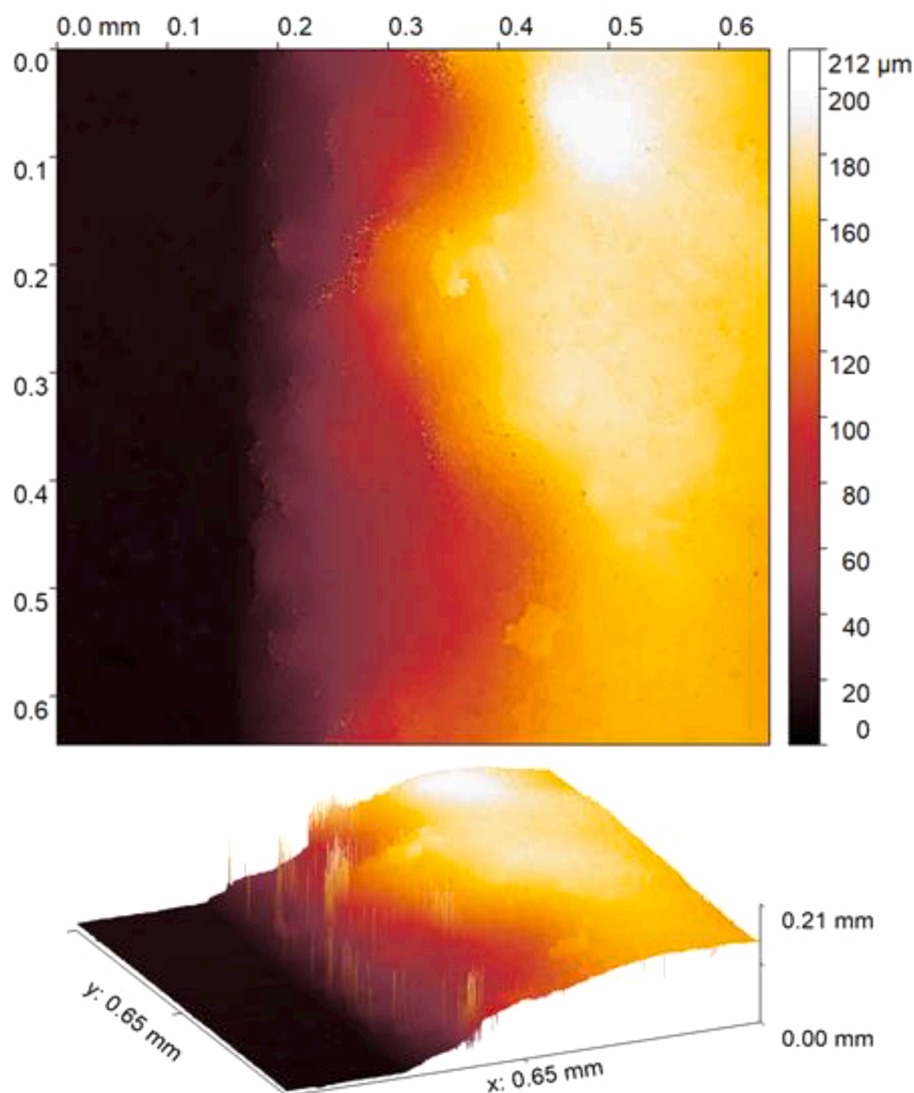

Fig. 9. Confocal height profile of the 3D printed layer with 500 mm·s^{-1} scan speed and the power laser of 5 W.

changing the ink composition and laser sintering parameters we obtained microstructures with different porosities. The ceramic-to-polymer weight ratio of 2:1 was selected to fabricate the porous microstructure (30 - 35 %), however, with the 4:1 loading, the dense microstructure was obtained (porosity of ~18.8 %). Layers of 2:1 ratio ink, sintered with the 5 W laser beam power had a well-sintered porous microstructure and were single-phase, as confirmed by XRD analysis. The fabricated layers were 143 ± 3 μm thick. Most importantly, the method developed reduces the sintering time required by other fabrication techniques from the range of 12 – 6 h [45] to 2 seconds, by utilizing the scanning speed of 500 mm·s^{-1}. Comparing the energy consumption, traditional sintering in a lab furnace (e.g., Carbolite Gero 30-3000, 2.9 kW) consumes about 2.3 kWh more per hour than laser sintering with a Fiber Laser (0.6 kW). Given that furnace sintering takes 4 to 48 h, while laser sintering takes only seconds, the shortened sintering time significantly reduces energy consumption, lowering costs and making the process more eco-friendly.

CRediT authorship contribution statement

Joanna Pośpiech: Writing – original draft, Visualization, Methodology, Investigation, Formal analysis, Data curation, Conceptualization. **Małgorzata Nadolska:** Writing – review & editing, Methodology, Formal analysis, Conceptualization. **Mateusz Cieślik:** Validation, Software. **Tomasz Sobczyk:** Software, Methodology. **Marek Chmielewski:** Software, Methodology. **Aleksandra Mielewczyk-Gryń:** Writing – review & editing, Supervision. **Ragnar Strandbakke:** Writing – review & editing, Project administration, Funding acquisition. **José Manuel Serra:** Project administration, Funding acquisition. **Sebastian Lech Wachowski:** Writing – review & editing, Supervision, Project administration, Investigation, Funding acquisition, Conceptualization.

Declaration of competing interest

The authors declare that they have no known competing financial interests or personal relationships that could have appeared to influence the work reported in this paper.

Data availability

Data will be made available on request.

Acknowledgments

Supplementary materials

Supplementary material associated with this article can be found, in the online version, at doi:10.1016/j.apmt.2024.102398.

References

[1] S. Choi, C.J. Kucharczyk, Y. Liang, X. Zhang, I. Takeuchi, H.Il Ji, S.M. Haile, Exceptional power density and stability at intermediate temperatures in protonic ceramic fuel cells, Nature Energy 3 (2018) 202–210.

[2] C. Duan, R.J. Kee, H. Zhu, C. Karakaya, Y. Chen, S. Ricote, A. Jarry, E.J. Crumlin, D. Hook, R. Braun, N.P. Sullivan, R. O'Hayre, Highly durable, coking and sulfur tolerant, fuel-flexible protonic ceramic fuel cells, Nature 557 (2018) 217–222.

[3] C. Duan, R. Kee, H. Zhu, N. Sullivan, L. Zhu, L. Bian, D. Jennings, R. O'Hayre, Highly efficient reversible protonic ceramic electrochemical cells for power generation and fuel production, Nature Energy 4 (2019) 230–240.

[4] E. Vøllestad, R. Strandbakke, M. Tarach, D. Catalán-Martínez, M.L. Fontaine, D. Beeaff, D.R. Clark, J.M. Serra, T. Norby, Mixed proton and electron conducting double perovskite anodes for stable and efficient tubular proton ceramic electrolysers, Nat. Mater. 18 (2019) 752–759.

[5] H. Iwahara, H. Uchida, N. Maeda, High temperature fuel and steam electrolysis cells using proton conductive solid electrolytes, J. Power Sources 7 (1982) 293–301.

[6] Suk-Won Ryan O'hayre, Whitney Cha, F.B.P. Colella, Fuel cell fundamentals, John Wiley & Sons, 2016.

[7] H. Iwahara, Hydrogen pumps using proton-conducting ceramics and their applications, Solid State Ionics 125 (1999) 271–278.

[8] T. Sakai, K. Isa, M. Matsuka, T. Kozai, Y. Okuyama, T. Ishihara, H. Matsumoto, Electrochemical hydrogen pumps using Ba doped LaYbO3 type proton conducting electrolyte, Int. J. Hydrogen Energy 38 (2013) 6842–6847.

[9] K.D. Kreuer, Proton conductivity: Materials and applications, Chem. Mater. 8 (1996) 610–641.

[10] T. Norby, Solid-state protonic conductors: Principles, properties, progress and prospects, Solid State Ionics 125 (1999) 1–11.

[11] I. Szpunar, R. Strandbakke, M.H. Sørby, S.L. Wachowski, M. Balaguer, M. Tarach, J. M. Serra, A. Witkowska, E. Dzik, T. Norby, M. Gazda, High-Temperature Structural and Electrical Properties of Ba Ln Co 2 O 6 Positrodes (2020) 1–18.

[12] J. Kim, S. Sengodan, G. Kwon, D. Ding, J. Shin, M. Liu, G. Kim, Triple-Conducting Layered Perovskites as Cathode Materials for Proton-Conducting Solid Oxide Fuel Cells, ChemSusChem 7 (2014) 2811–2815.

[13] D. Cao, M. Zhou, X. Yan, Z. Liu, J. Liu, High performance low-temperature tubular protonic ceramic fuel cells based on barium cerate-zirconate electrolyte, Electrochem. Commun. 125 (2021) 106986.

[14] C. Duan, J. Huang, N. Sullivan, R. O'Hayre, Proton-conducting oxides for energy conversion and storage, Appl. Phys. Rev. 7 (2020).

[15] S.S. Shin, J.H. Kim, K.T. Bae, K.T. Lee, S.M. Kim, J.W. Son, M. Choi, H. Kim, Multiscale structured low-temperature solid oxide fuel cells with 13 W power at 500 °c, Energy and Environmental Science 13 (2020) 3459–3468.

[16] Quina, I., Almar, L., Norby, T., Escola, S., Quina, I., Almar, L., Catala, D., Norby, T., Escola, S., *Article Direct electrocatalytic CO 2 reduction in a pressurized tubular protonic membrane reactor Direct electrocatalytic CO 2 reduction in a pressurized tubular protonic membrane reactor*, (2023).

[17] E. Vøllestad, Tubular protonic ceramic electrolysis cells and direct hydrogen compression. High-Temperature Electrolysis, IOP Publishing, 2023, 13–1 to 13–17.

[18] Z. Chen, Z. Li, J. Li, C. Liu, C. Lao, Y. Fu, C. Liu, Y. Li, P. Wang, Y. He, 3D printing of ceramics: A review, J. Eur. Ceram. Soc. 39 (2019) 661–687.

[19] L. Zeng, P. Li, Y. Yao, B. Niu, S. Niu, B. Xu, Recent progresses of 3D printing technologies for structural energy storage devices, Materials Today Nano 12 (2020) 1–13.

[20] W. Zhang, H. Liu, X. Zhang, X. Li, G. Zhang, P. Cao, 3D Printed Micro-Electrochemical Energy Storage Devices: From Design to Integration, Adv. Funct. Mater. 31 (2021) 1–40.

[21] L. Zheng, R. Xu, J. Zhang, F. Yu, C. Li, J. Sunarso, W. Zhang, X. Meng, N. Yang, Enhanced electrochemical performance by structural design of electrolyte surface combining 3D printing technology with multi-physical modelling, Chem. Eng. J. 451 (2023).

[22] M. Lira, N. Kostretsova, I. Babeli, L. Bernadet, S. Marquez, A. Morata, M. Torrell, A. Tarancón, Large-area 3D printed electrolyte-supported reversible solid oxide cells, Electrochim. Acta 467 (2023).

[23] S. Zarabi Golkhatmi, P.D. Lund, M.I. Asghar, A novel CuFe2O4 ink for the fabrication of low-temperature ceramic fuel cell cathodes through inkjet printing, Materials Advances 5 (2023) 143–158.

[24] A.G. Sabato, M. Nuñez Eroles, S. Anelli, C.D. Sierra, J.C. Gonzalez-Rosillo, M. Torrell, A. Pesce, G. Accardo, M. Casas-Cabanas, P. López-Aranguren, A. Morata, A. Tarancón, 3D printing of self-supported solid electrolytes made of glass-derived Li1.5Al0.5Ge1.5P3O12 for all-solid-state lithium-metal batteries, J. Mater. Chem. A 11 (2023) 13677–13686.

[25] U. Scheithauer, E. Schwarzer, H.J. Richter, T. Moritz, Thermoplastic 3D printing - An additive manufacturing method for producing dense ceramics, Int. J. Appl. Ceram. Technol. 12 (2015) 26–31.

[26] S. Tagliaferri, A. Panagiotopoulos, C. Mattevi, Direct ink writing of energy materials, Materials Advances 2 (2021) 540–563.

[27] M. Zhou, W. Liu, H. Wu, X. Song, Y. Chen, L. Cheng, F. He, S. Chen, S. Wu, Preparation of a defect-free alumina cutting tool via additive manufacturing based on stereolithography – Optimization of the drying and debinding processes, Ceram. Int. 42 (2016) 11598–11602.

[28] S. Nachum, J. Vogt, F. Raether, Additive manufacturing of ceramics: Stereolithography versus binder jetting, 93, CFI Ceram. Forum Int. (2016) E27–E33.

[29] J. Grau, J. Moon, High green density ceramic components fabricated by the slurry-based 3DP process, Solid Freeform Fabrication Proceedings (1997) 371–378.

[30] A.N. Chen, J.M. Wu, K. Liu, J.Y. Chen, H. Xiao, P. Chen, C.H. Li, Y.S. Shi, High-performance ceramic parts with complex shape prepared by selective laser sintering: a review, Advances in Applied Ceramics 117 (2018) 100–117.

[31] L.C. Hwa, S. Rajoo, A.M. Noor, N. Ahmad, M.B. Uday, Recent advances in 3D printing of porous ceramics: A review, Curr. Opin. Solid State Mater. Sci. 21 (2017) 323–347.

[32] T.D. Ngo, A. Kashani, G. Imbalzano, K.T.Q. Nguyen, D. Hui, Additive manufacturing (3D printing): A review of materials, methods, applications and challenges, Composites Part B: Engineering 143 (2018) 172–196.

[33] S. Mu, Z. Zhao, H. Huang, J. Lei, F. Peng, H. Xiao, S Kyle, J. Brinkman, T. Joshua, Advanced Manufacturing of Intermediate-Temperature Protonic Ceramic Electrochemical Cells, The Electrochemical Society Interface 29 (2020) 67–73.

[34] S. Mu, Y. Hong, H. Huang, A. Ishii, J. Lei, Y. Song, Y. Li, K.S. Brinkman, F. Peng, H. Xiao, J. Tong, A novel laser 3D printing method for the advanced manufacturing of protonic ceramics, Membranes 10 (2020) 1–17.

[35] M. Zou, J. Conrad, B. Sheridan, J. Zhang, H. Huang, S. Mu, T. Zhou, Z. Zhao, K. S. Brinkman, H. Xiao, F. Peng, J. Tong, 3D Printing Enabled Highly Scalable Tubular Protonic Ceramic Fuel Cells, ACS Energy Letters 8 (2023) 3545–3551.

[36] W. Huang, C. Finnerty, R. Sharp, K. Wang, B. Balili, High-Performance 3D Printed Microtubular Solid Oxide Fuel Cells, Advanced Materials Technologies 2 (2017).

[37] I. Szpunar, R. Strandbakke, M.H. Sørby, S.L. Wachowski, M. Balaguer, M. Tarach, J. M. Serra, A. Witkowska, E. Dzik, T. Norby, M. Gazda, A. Mielewczyk-Gryń, High-temperature structural and electrical properties of BaLnCo2O6 positrodes, Materials 13 (2020) 1–18.

[38] I. Szpunar, S. Wachowski, T. Miruszewski, K. Dzierzgowski, K. Górnicka, T. Klimczuk, M.H. Sørby, M. Balaguer, J.M. Serra, R. Strandbakke, M. Gazda, A. Mielewczyk-Gryń, Electric and magnetic properties of lanthanum barium cobaltite, J. Am. Ceram. Soc. 103 (2020) 1809–1818.

[39] R. Zohourian, R. Merkle, G. Raimondi, J. Maier, Mixed-Conducting Perovskites as Cathode Materials for Protonic Ceramic Fuel Cells: Understanding the Trends in Proton Uptake, Adv. Funct. Mater. 28 (2018) 1801241.

[40] R. Pelosato, G. Cordaro, D. Stucchi, C. Cristiani, G. Dotelli, Cobalt based layered perovskites as cathode material for intermediate temperature Solid Oxide Fuel Cells: A brief review, J. Power Sources 298 (2015) 46–67.

[41] E. Vøllestad, M. Schrade, J. Segalini, R. Strandbakke, T. Norby, Relating defect chemistry and electronic transport in the double perovskite Ba1-xGd0.8La0.2+xCo2O6-δ (BGLC), J. Mater. Chem. A 5 (2017) 15743–15751.

[42] G. Raimondi, F. Giannici, A. Longo, R. Merkle, A. Chiara, M.F. Hoedl, A. Martorana, J. Maier, X-ray spectroscopy of (Ba,Sr,La)(Fe,Zn,Y)O3-δIdentifies structural and electronic features favoring proton uptake, Chem. Mater. 32 (2020) 8502–8511.

[43] R. Merkle, M.F. Hoedl, G. Raimondi, R. Zohourian, Oxides with mixed protonic and electronic conductivity, Annu. Rev. Mater. Res. 51 (2021) 461–493.

[44] S.L. Wachowski, I. Szpunar, M.H. Sørby, A. Mielewczyk–Gryń, M. Balaguer, C. Ghica, M.C. Istrate, M. Gazda, A.E. Gunnæs, J.M. Serra, T. Norby, R. Strandbakke, Structure and water uptake in BaLnCo2O6−δ (Ln =La, Pr, Nd, Sm, Gd, Tb and Dy), Acta Mater. 199 (2020) 297–310.

[45] D. Gierszewska, I. Szpunar, F. Oseko, J. Pospiech, M. Nadolska, M. Pieragowska, K. Reniecka, K. Waniek, K. Leszczynski, M.G. Aleksandra Mielewczyk-Gryn, Microstructural Design of Ba0.5La0.5Co0.5Fe0.5O3 Perovskite Ceramics, Materials 14 (2021) 4656.

[46] S. Wachowski, I. Szpunar, D. Balcerzak, J. Pośpiech, A. Mielewczyk-Gryń, M. Nadolska-Dawidowska, M. Gazda, M. Balaguer, J.M. Serra, Einar Vøllestad, T.N. and R.S., *Influence of iron content on electrocatalytic properties of Ba0.5La0.5Co1-xFexO3-δ (0≤x≤1) as positrode for proton ceramic electrochemical cells*, n.d.

[47] A. Løken, S. Ricote, S. Wachowski, Thermal and Chemical Expansion in Proton Ceramic Electrolytes and Compatible Electrodes, cryst. 8 (2018) 365.

[48] Erik van der Zalm, Marlin Firmware (2011).

[49] B.V. Ultimaker, UltiMaker Cura (2023).

[50] W.S. Rasband, Image J (1997).